buildings

MDPI

Article

Influence of Compressive Strength and Steel-Tube Thickness on Axial Compression Performance of Ultra-High-Performance Concrete-Filled Stainless-Steel Tube Columns Containing Coarse Aggregates

Wenrui Li [1], Mengqi Zhu [2], Guo Li [1], Yang Hu [1], Bei Wang [1], Yongfei Cao [1], Wenting He [3], Haiyang Li [4], Zhaopeng Tang [4] and Yingda Zhang [4,*]

[1] The First Construction Engineering Limited Company of China Construction Third Engineering Bureau (Sichuan Branch), Chengdu 641400, China
[2] Dongfang Boiler Co., Ltd., Chengdu 611731, China
[3] Centre for Infrastructure Engineering and Safety, School of Civil and Environmental Engineering, The University of New South Wales, Sydney, NSW 2052, Australia; wenting.he@unsw.edu.au
[4] School of Architecture and Civil Engineering, Xihua University, Chengdu 610039, China
* Correspondence: yingda.zhang@xhu.edu.cn

Abstract: With the increasing use of concrete-filled steel tubular (CFST) structures, exposed steel tubes are highly susceptible to corrosion, posing potential safety hazards. This study innovatively proposes the use of stainless-steel tubes instead of traditional carbon-steel ones and introduces coarse aggregates into ultra-high-performance concrete (UHPC), forming a coarse aggregate-incorporated ultra-high-performance concrete-filled stainless-steel tube (CA-UFSST). The inclusion of coarse aggregates not only compensates for the shortcomings of UHPC but also enhances the overall mechanical performance of the composite structure. Twenty sets of specimens were designed to analyze the influence of four parameters, including the coarse aggregate content, compressive strength, stainless-steel-tube thickness, and stainless-steel type on the axial compression performance of UHPC. The experimental results indicate that the failure mode of UHPC is related to the confinement ratio. As the confinement ratio increases, the failure mode transitions from shear failure to bulging failure. The addition of coarse aggregates enhances the stiffness of the specimens. Furthermore, this paper discusses the applicability of six current codes in predicting the bearing capacity of CA-UFSST and finds that the European code exhibits the best prediction performance. However, as the confinement ratio increases, the prediction accuracy becomes notably insufficient. Therefore, it is necessary to establish a more accurate calculation model for the axial compression bearing capacity.

Keywords: concrete stainless-steel tube; CA-UFSST; confinement coefficient; analytical model; bearing capacity

Citation: Li, W.; Zhu, M.; Li, G.; Hu, Y.; Wang, B.; Cao, Y.; He, W.; Li, H.; Tang, Z.; Zhang, Y. Influence of Compressive Strength and Steel-Tube Thickness on Axial Compression Performance of Ultra-High-Performance Concrete-Filled Stainless-Steel Tube Columns Containing Coarse Aggregates. *Buildings* **2024**, *14*, 3605. https://doi.org/10.3390/buildings14113605

Academic Editor: Grzegorz Ludwik Golewski

Received: 14 October 2024
Revised: 5 November 2024
Accepted: 9 November 2024
Published: 13 November 2024

1. Introduction

With the advancement of science and technology, and in pursuit of vigorously promoting the process of high-quality, energy-efficient development, the fields of architecture and civil engineering have paid keen attention to issues such as structural safety, cost-effectiveness, and compliance with sustainable development requirements. Consequently, the structures of various buildings have begun to trend towards larger scales, greener designs, and lighter weights. Traditional reinforced concrete structures and steel structures have struggled to adapt to increasingly complex service environments and application forms, leading to a growing adoption of the concrete-filled steel-tube (CFST) composite structure [1]. Compared to traditional reinforced concrete and steel structures, CFSTs enhance the ductility of concrete through passive confinement, thereby improving the structural bearing capacity while also serving as concrete formwork. Moreover, the core

concrete effectively restrains the local buckling of the steel tube [2]. Therefore, the CFST structure aligns well with the current trend of high-strength, high-performance engineering structures.

CFSTs also have their inherent limitations. Firstly, under service conditions in bridges and ports, exposed steel tubes are highly susceptible to corrosion. The loss of the cross-sectional area of the steel tube can lead to a reduction in the confinement degree and even stress concentration, ultimately posing safety risks to the structure [3]. Secondly, after yielding, carbon steel exhibits strain-softening behavior, which is not ideal for confining high-strength concrete. With the continuous evolution of technological materials, ultra-high-performance concrete (UHPC), characterized by high strength and high toughness, has gradually replaced ordinary concrete in combination with steel tubes, forming UHPC-filled steel tubes (UFSTs) [4,5]. While this further enhances the structural performance, it also introduces new challenges. For instance, due to the relatively small difference in the elastic modulus between UHPC and ordinary concrete, the reduction in size of a section of a composite structure does not meet expectations while maintaining equivalent stiffness. Furthermore, the cost of UHPC is excessively high, leading to difficulties in its widespread application. Chen et al. [6] proved that the restraint effect of steel tube on UHPC is not as significant as that on ordinary concrete. Guler et al. [7] carried out an axial compression test of the UHPC short column of a round steel pipe. As the wall thickness of the steel tube increased from 2.5 mm to 3.65 mm, the ductility coefficient and the bearing capacity improvement coefficient increased by 69% and 5% on average, respectively, indicating that an increase in steel-tube thickness had a greater impact on ductility than the bearing capacity. Xu et al. [8] and Le Hoang et al. [9], respectively, conducted axial compression tests on UHPC short-column specimens of circular steel tubes and found that an improvement in the bearing capacity and ductility of steel fibers was not obvious, and an increase in the restraint coefficient could significantly improve the overall performance of UHPC steel tubes. Consequently, these limitations restrict the further enhancement of the overall performance of UFSTs [10].

To address the aforementioned issues related to both the steel-tube and the core concrete, some researchers have proposed using stainless-steel tubes as a substitute for traditional carbon steel, forming a concrete-filled stainless-steel-tube (CFSST) composite structure [11]. This approach aims to counteract the impact of adverse external environmental conditions on the performance of the composite structure. Due to the presence of certain alloy elements in its composition, the stress–strain curve of stainless-steel material differs from that of ordinary carbon steel [12]. In the stress–strain curve of stainless steel, the proportional limit is low, and the yield platform is not obvious, and the stress when the strain reaches 0.2% is often used as its nominal yield strength, and it shows obvious nonlinear characteristics from the initial loading. Unlike the softening behavior of carbon steel, stainless steel exhibits strain hardening after yielding, and its elongation can reach approximately twice that of low-carbon steel. The strength of different stainless steels varies significantly. Stainless steel has many excellent engineering characteristics, such as corrosion protection, aesthetics, good fire resistance and durability, high ductility and good impact fatigue resistance, lower long-term maintenance costs, and a longer service life [13]. Currently, the stainless steels widely used in engineering include austenitic, duplex, and ferritic types [14,15]. Among them, duplex stainless steel has a nominal yield strength much higher than that of austenitic and ferritic stainless steels, ranging from 450 to 550 MPa. Young et al. [16] and Ellobody et al. [17] conducted an experimental study on thin-walled concrete stainless-steel tubes with two cross-sections, namely, rectangular steel tubes made of cold-formed high-strength stainless steel with a yield of strength up to 536 MPa. Lam and Gardne [18] supplemented the study of concrete stainless-steel tubes with a circular section, expanded the strength grade range of the concrete to 30–80 MPa, and compared the test results with specifications. The results show that the predicted results of the European specification EC4 and the American specification ACI were conservative. Tao et al. [19] and Dai et al. [20] carried out experiments on circular- and square-section

stainless-steel tubular concrete columns, respectively. Control parameters were selected, such as the section size, type and grade of stainless steel, concrete type, strength and age, width-to-thickness ratio, etc. The results show that the bonding property of stainless-steel tubes is lower than that of ordinary carbon-steel tubes. Despite their superior mechanical properties, the high cost of UHPC and stainless steel presents a significant challenge for their widespread application. The use of UHPC and stainless steel in CA-UFSST columns needs to be economically viable, considering factors such as material costs, construction efficiency, and life-cycle performance. Additionally, the sustainability of these materials should be evaluated, including their environmental impact during production, use, and disposal. Future research should explore cost-effective alternatives or recycling strategies to enhance the economic and environmental sustainability of CA-UFSST columns.

Meanwhile, incorporating coarse aggregates (typically limestone with a particle size of 5 to 10 mm) into UHPC can greatly compensate for its deficiencies, such as its high autogenous shrinkage and relatively low elastic modulus [21]. Research has shown that introducing coarse aggregates into UHPC not only maintains its high strength, toughness, durability, and ductility but also forms a rigid skeleton that significantly enhances its elastic modulus and reduces autogenous shrinkage by 20% to 38%. This modification substantially improves the compatibility between steel tubes and UHPC [22,23].

The existing design specifications for the axial compressive bearing capacity of CFST mainly include the following: a Chinese specification (CECS 159:2004) based on the superposition theory, a European specification (EC4), and an American specification (ACI 318-05); an American specification for the design of steel structures (AISC 360) based on the steel-analog theory; and Chinese specifications (GB 50936-2014 and DBJ/T13-51-2020) based on the unified theory. However, these specifications impose certain limits on the maximum values of steel-tube and concrete strength. Thus, whether they can be directly applied to predict the bearing capacity of UFSSTs needs to be verified.

Based on the aforementioned background, it is clear that with the widespread application of CFST structures in civil engineering, the corrosion resistance issues of conventional carbon-steel tubes have become increasingly prominent. Concurrently, the introduction of UHPC has posed new challenges. As such, this study aims to investigate the axial compressive behavior of a novel structure combining UHPC with stainless-steel tubes, denoted as a coarse aggregate-incorporated ultra-high-performance concrete-filled stainless-steel tube (CA-UFSST), with the objective of providing theoretical support for engineering practices. Axial compression tests were conducted to investigate the influence of the coarse aggregate content, concrete strength, and stainless-steel-tube thickness and type on the axial compression performance of these short columns. By analyzing the failure phenomena of the test specimens, as well as their load–displacement curves and load–strain curves, the mechanical mechanism of these components is explored. Furthermore, several bearing capacity calculation models from existing standards are used to compare the experimental results.

2. Experimental Program

2.1. Material Properties

In this experiment, two types of stainless-steel tubes were used, including square cold-drawn seamless austenitic stainless-steel tubes produced by Taizhou Mobei Stainless Steel Co., Ltd. (Taizhou, China) and square cold-drawn seamless Duplex stainless-steel tubes produced by Xinghua Shengteng Metal Products Co., Ltd. (Xinghua, China). The material properties of the stainless-steel tubes were tested according to GB/T 228.1-2010 [24]. Three sets of standard dog-bone specimens were cut from different types and thicknesses of stainless-steel tubes using wire cutting, and both transverse and longitudinal strain gauges were placed in the middle of each specimen. The reasons for choosing austenitic stainless steel and duplex stainless steel lie in their excellent corrosion resistance and mechanical properties, particularly when used as alternatives to traditional carbon-steel tubes to mitigate corrosion issues in environments such as bridges and ports. Unlike ordinary carbon steel, stainless steel exhibits distinct mechanical characteristics, notably its

strain-hardening behavior post-yield, which is highly beneficial for confining high-strength concrete. Austenitic stainless steel is distinguished by its superior ductility, allowing it to sustain significant deformation even after yielding. On the other hand, duplex stainless steel is characterized by its high strength, with a yield strength markedly higher than that of austenitic and ferritic stainless steels. The measured mechanical properties and stress–strain curves of the stainless steel are presented in Table 1.

Table 1. Mechanical properties of stainless-steel tubes.

Stainless-Steel Tubes	t_{test}/mm	$\sigma_{0.2}$/MPa	σ_u/MPa	E_s/MPa	v
Austenitic	2.9	468	587.4	207.8	0.31
	6.3	509	649.5	198.3	0.29
	10.1	525	674.9	203.1	0.32
Duplex	9.8	817	886.3	212.6	0.3

Note: $\sigma_{0.2}$/MPa signifies the yield strength; σ_u/MPa represents the tensile strength of the specimen; E_s/MPa denotes the elastic modulus; and v stands for Poisson's ratio.

The core concrete of the specimens can be divided into three strength grades, all prepared using ready-mix materials, steel fibers, and coarse aggregates provided by SBT-UDC (II) from Jiangsu Suebot New Materials Co., Ltd. (Nanjing, China). Specifically, fiber-reinforced concrete (FRC) with a strength grade of C80 differs from the ready-mix material used in UHPC, while UHPC with strength grades of U100 and U120 differ in the type of steel fibers used; the former employs regular steel fibers, while the latter utilizes copper-coated straight steel fibers. The coarse aggregate consisted of limestone particles with a diameter of 5–10 mm, which were washed with clean water before casting. This selection was based on the ability of coarse aggregates to effectively compensate for the deficiencies of UHPC while maintaining its high strength, high toughness, durability, and ductility. The size of aggregate directly affects the mechanical properties of UHPC. Larger aggregates can provide better skeleton support and enhance the compressive strength and stiffness of the concrete. The mix proportions for different types of core concrete are shown in Table 2. Concrete material property tests were conducted in accordance with GB/T 50081-2019 [25]. The measured mechanical properties of the concrete are presented in Table 3.

Table 2. Concrete mix design proportions (kg/m^3).

Concrete	Pre-Mix 1	Pre-Mix 2	Water	CA	Regular Steel Fibers	Copper-Coated Straight Steel Fibers
FRC80	1065	-	149.1	1065	53.25	-
UHPC100-CA	-	1065	138.45	1065	74.55	-
UHPC100	-	2130	223.65	-	106.5	-
UHPC120-CA	-	1207	150.88	905.25	-	100.18
UHPC120	-	2130	213	-	-	142.71

Note: CA represents the coarse aggregate.

Table 3. Mechanical properties of the concrete.

Core Concrete	f_{cu}/MPa	f_{ck}/MPa	E_c/MPa
FRC80	100.78	90.7	37,600
UHPC100-CA	110.89	99.8	52,400
UHPC100	107.78	97	43,700
UHPC120-CA	117.11	105.4	53,200
UHPC120	114.11	102.7	44,200

Note: f_{cu}/MPa represents the compressive strength of a 100 mm × 100 mm × 100 mm cubic specimen; f_{ck}/MPa denotes the standard value of the axial compressive strength for a 100 mm × 100 mm × 300 mm prismatic specimen; and E_c/MPa indicates the elastic modulus of the concrete.

2.2. Design and Fabrication of Test Specimens

In this experiment, a total of 20 square short-column specimens were designed and fabricated for axial compression tests. These include 8 short columns of CA-UFSST, 8 short columns of UFSST, and 4 short columns of conventional fiber-reinforced concrete-filled stainless-steel tubes (CFSSTs). The experimental variables include the coarse aggregate content and compressive strength of the core concrete, as well as the wall thickness and type of stainless steel used for the tubes. The aspect ratio (L/D) was set at 3 to simultaneously avoid global instability and end effects [26]. To eliminate the influence of welds, seamless stainless-steel tubes were selected, each with a cross-section of 100 mm × 100 mm and wall thicknesses (t) that incrementally increased to 3 mm, 6 mm, and 10 mm. The core ultra-high-performance concrete in the CA-UFSST and UFSST specimens exhibited compressive strengths of 100 MPa and 120 MPa, respectively, while the control group of CFSST specimens were uniformly filled with FRC with a compressive strength of 80 MPa.

The relevant parameters of the specimens are presented in Table 4. In the specimen numbering, the letters 'A' and 'D' denote austenitic stainless steel and duplex stainless steel, respectively. The numbers following the letters 't' and 'c' represent the nominal thickness of the stainless-steel tubes and the strength of the core concrete, respectively. The suffix 'CA' indicates that the core concrete contains coarse aggregates. Figure 1 provides a cast process of the test specimens' fabrication. First, the stainless-steel tubes were cut to the designated height, and both ends were meticulously ground to ensure perpendicularity. Prior to concrete pouring, the interior and exterior surfaces of the tube were thoroughly cleaned to remove any dust and oil, and a film was affixed at the bottom to prevent grout leakage. Subsequently, based on the specified core concrete strength grade, the stainless-steel tubes were placed in batches on a vibrating table and pour the core concrete in layers. During the pouring process, three sets of standard cubic specimens for testing were reserved, and a vibrator was used to ensure the compactness of the concrete. It was essential to maintain a concrete level that was slightly above the top surface of the stainless-steel tubes, by approximately 1–2 cm, to minimize the impact of concrete shrinkage on the experiment during curing. The specimens were allowed to undergo natural curing indoors for 28 days. Once cured, an angle grinder was used to smooth off any excess concrete from both ends, until they were flush with the stainless-steel tube, and then, grid lines were marked, as required.

Table 4. Parameters related to test specimens.

ID	Type of Stainless-Steel Tubes	t_e /mm	$\sigma_{0.2}$ /MPa	Type of Concrete	f_{cu} /MPa	Confinement Coefficient ξ
A-t3c80-CA	A	2.9	468	FRC80	100.78	0.68
A-t6c80-CA	A	6.3	509			1.63
A-t10c80-CA	A	10.1	525			3.26
D-t10c80-CA	D	9.8	817			5.07
A-t3c100-CA	A	2.9	468	UHPC100-CA	110.89	0.62
A-t6c100-CA	A	6.3	509			1.49
A-t10c100-CA	A	10.1	525			2.96
D-t10c100-CA	D	9.8	817			4.60
A-t3c100	A	2.9	468	UHPC100	107.78	0.64
A-t6c100	A	6.3	509			1.53
A-t10c100	A	10.1	525			3.04
D-t10c100	D	9.8	817			4.74
A-t3c120-CA	A	2.9	468	UHPC120-CA	117.11	0.58
A-t6c120-CA	A	6.3	509			1.41
A-t10c120-CA	A	10.1	525			2.80
D-t10c120-CA	D	9.8	817			4.36
A-t3c120	A	2.9	468	UHPC120	114.11	0.60
A-t6c120	A	6.3	509			1.44
A-t10c120	A	10.1	525			2.88
D-t10c120	D	9.8	817			4.47

Note: A and D denote austenitic and duplex stainless steel, respectively; t represents the nominal thickness of the stainless-steel tube; c denotes the strength of the core concrete; and CA indicates concrete mixes with coarse aggregates.

Figure 1. Cast of test specimens.

2.3. Loading Device and Measurement Layout

The axial compression test was conducted on a 5000 kN electro-hydraulic servo-controlled testing machine with a precision of 1 N. Two sets of 50 mm-range Linear Variable Differential Transformers (LVDTs) were placed on both sides of the specimen to monitor its longitudinal deformation and compression status. A schematic diagram of the loading setup and an on-site photograph are presented in Figure 2a. The data collection points on the stainless-steel tubes are illustrated in Figure 2b. Six sets of transverse and longitudinal strain gauges were attached to the adjacent rectangular surfaces of the specimen, specifically at the top, middle, and bottom positions. The transverse strain gauges, designated with odd numbers, were used to capture the hoop strain induced by the core concrete's compression on the stainless-steel tubes, thereby assessing the confinement effect of the tubes on the core concrete. The axial strain gauges, designated with even numbers, were employed to analyze the development of the axial compressive deformation and local buckling of the stainless-steel tubes [27].

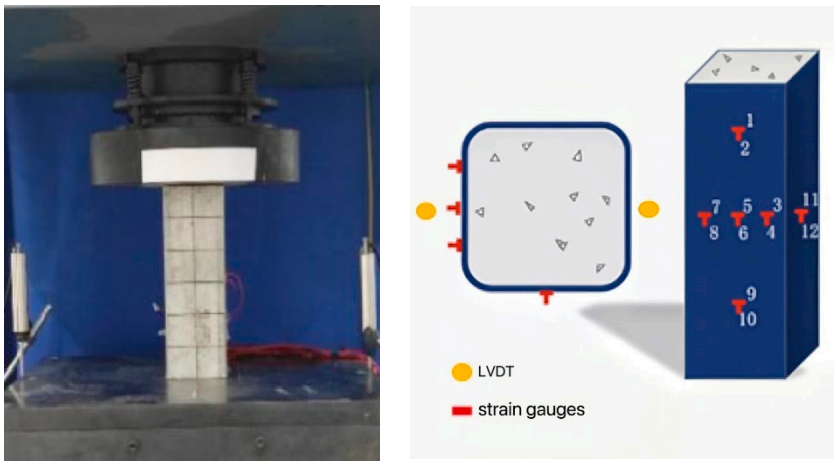

(**a**) (**b**)

Figure 2. (**a**) Loading configuration; (**b**) measurement layouts.

To verify the instrument functionality and ensure proper alignment of the specimen, a preload was applied before the commencement of the axial compression test. It was crucial to maintain a difference of less than 5% between the readings of the two LVDTs and their average value, thereby preventing the occurrence of eccentric loading. The preload was set to a target load of 300 kN to avoid any damage to the specimen. The test was conducted under displacement-controlled loading with a rate of 0.5 mm/min. The axial loading test was terminated when the load dropped to 75% of the ultimate load or when the axial compressive deformation reached 18 mm.

3. Test Results and Discussions

3.1. Failure of Specimen

The complete loading process of a typical test specimen in this experiment, exemplified by the axial compression failure of the specimen A-t3c80-CA, is shown in Figure 3. In the initial stage, there was no interaction between the stainless-steel tube and the concrete, and the specimen exhibited no significant noise or deformation, as depicted in Figure 3a. When loaded to approximately 80% of the measured ultimate load, the core concrete emitted sounds of fragmentation and steel fiber pull-out, accompanied by the initiation and propagation of unstable cracks. At this point, the stainless-steel tube began to exert a gradually increasing confining effect, resulting in the appearance of minute folds on its four planar surfaces, as illustrated in Figure 3b. As the axial displacement of the specimen A-t3c80-CA continued to increase, the concrete cracks expanded and eventually coalesced, producing a distinct sound accompanied by the snapping of steel fibers, indicating that the specimen had reached its ultimate load, as shown in Figure 3c. Subsequently, the bearing capacity continued to decline, with the stainless-steel tube exhibiting significant buckling. The folds extended to the corners, forming continuous inclined annular folds. Finally, the stainless steel tore at the corners due to excessive circumferential stress, as depicted in Figure 3d.

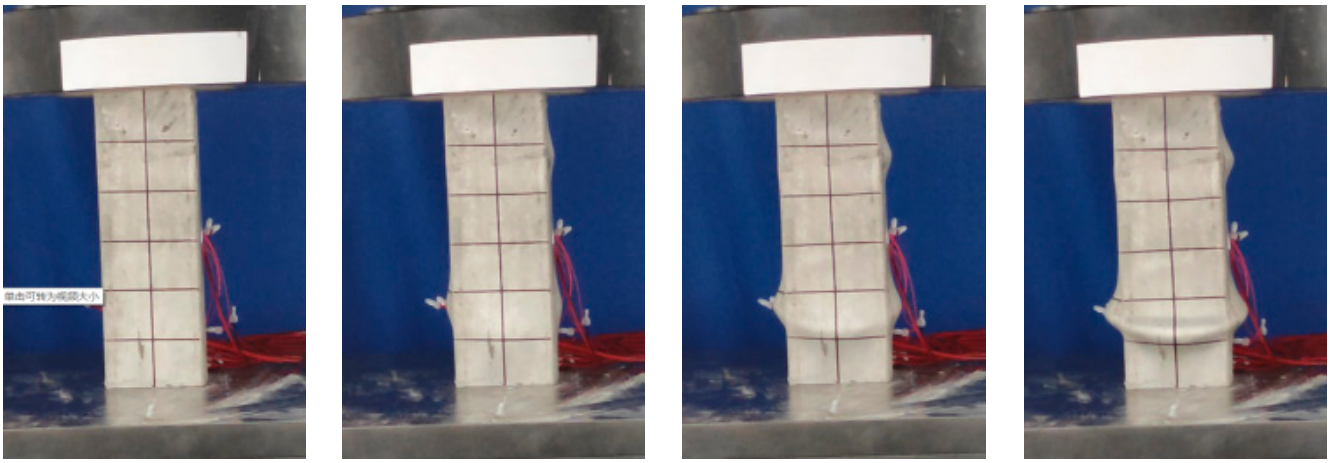

(**a**) Δ = 5 mm (**b**) Δ = 10 mm (**c**) Δ = 15 mm (**d**) Δ = 20 mm

Figure 3. Failure process of test specimen A-t3c80-CA.

For specimens with a confinement coefficient ranging from 0.58 to 1.63, subtle folds began to appear around the perimeter of the external stainless-steel tube, as the specimen approached its ultimate bearing capacity. These folds gradually widened and extended to the corners, forming continuous annular bulges as the deformation of the specimen intensified and the core concrete cracked. The inclined degree of the annular bulge bands varied among different specimens, with angles being between 30 and 45 degrees from the horizontal. Furthermore, as the confinement coefficient increased, the bulging state gradually transitioned from sharp to rounded. Eventually, tears appeared at the corners of the steel tube due to excessive transverse stress. For specimens with a confinement coefficient ranging from 2.80 to 5.06, the stainless-steel tube only exhibited insignificant local expansion or overall slight swelling at both ends, and no structural damage was observed in the appearance.

After the specimens were fully loaded, a handheld cutting machine was used to cut through the external stainless-steel tube of the typical specimens, in order to further clarify the damage to the core concrete under different parameter conditions. The failure modes of all specimens can be categorized into two types based on the cracking of the core concrete: diagonal shear failure and bulging failure. Diagonal shear failure is characterized by diagonal cracks through the concrete, whereas bulging failure is manifested by the

expansion of the stainless-steel tube due to confinement. Visual examples of these typical failure modes are shown in Figure 4.

(**a**) A-t6c100-CA (**b**) A-t6c100 (**c**) A-t3c120-CA (**d**) A-t3c100

Figure 4. Failure of core concrete.

3.2. Load–Displacement Curve

Figure 5 presents the load–displacement (N–Δ) curves for all square short-column specimens. Based on the development trend of N–Δ, these curves can be simplified into five development patterns, as shown in Figure 5a. The load–displacement curves can be divided into four stages: the elastic stage (segment OA), the elastoplastic stage (segment AB), the post-deformation stage (segment BC), and the strengthening/weakening stage (segment CD).

Elastic stage (segment OA): Before the loading reaches 70–80% of the ultimate load, the load–displacement curve is nearly a straight line. The bearing capacity is distributed in proportion to stiffness. At this point, the core concrete does not exhibit significant transverse deformation, and the stainless-steel tube does not have a notable confining effect on the core concrete. Comparing the tangent stiffness data of the specimens in Table 5, the addition of coarse aggregates increases the initial tangent stiffness (K_0) by an average of approximately 1.27 times and raises the corresponding load at the end of the elastic stage from 73% to around 82% of the ultimate load. This is attributed to the enhanced overall stiffness of the concrete resulting from the interlocking and engagement of coarse aggregates, forming a rigid skeleton. Additionally, the incorporation of coarse aggregates can bring the initial stiffness (K_0) of specimens with the same concrete strength closer together, even when the thickness of the stainless-steel tube varies. The effect of coarse aggregates on the mechanical behavior varies with the thickness of the stainless-steel tube. For specimens with a thin tube (e.g., t = 3 mm), the addition of coarse aggregates significantly increases the initial stiffness and delays the onset of plastic deformation, as evidenced by the extended elastic stage. However, for specimens with thicker tubes (e.g., t = 10 mm), the enhancement in stiffness is was less pronounced, as the tube itself provided sufficient confinement to the core concrete. Instead, the coarse aggregates primarily contributed to improving the ductility and energy absorption capacity of the specimens by providing additional resistance to crack propagation. The tangent stiffness (K_0) is defined by Equation (1).

$$K_0 = \frac{N_{0.45u}}{\Delta_{0.45t}} \tag{1}$$

where $N_{0.45t}$ represents the 45% ultimate bearing capacity, and $\Delta_{0.45t}$ represents the displacement value at 45% of N_t.

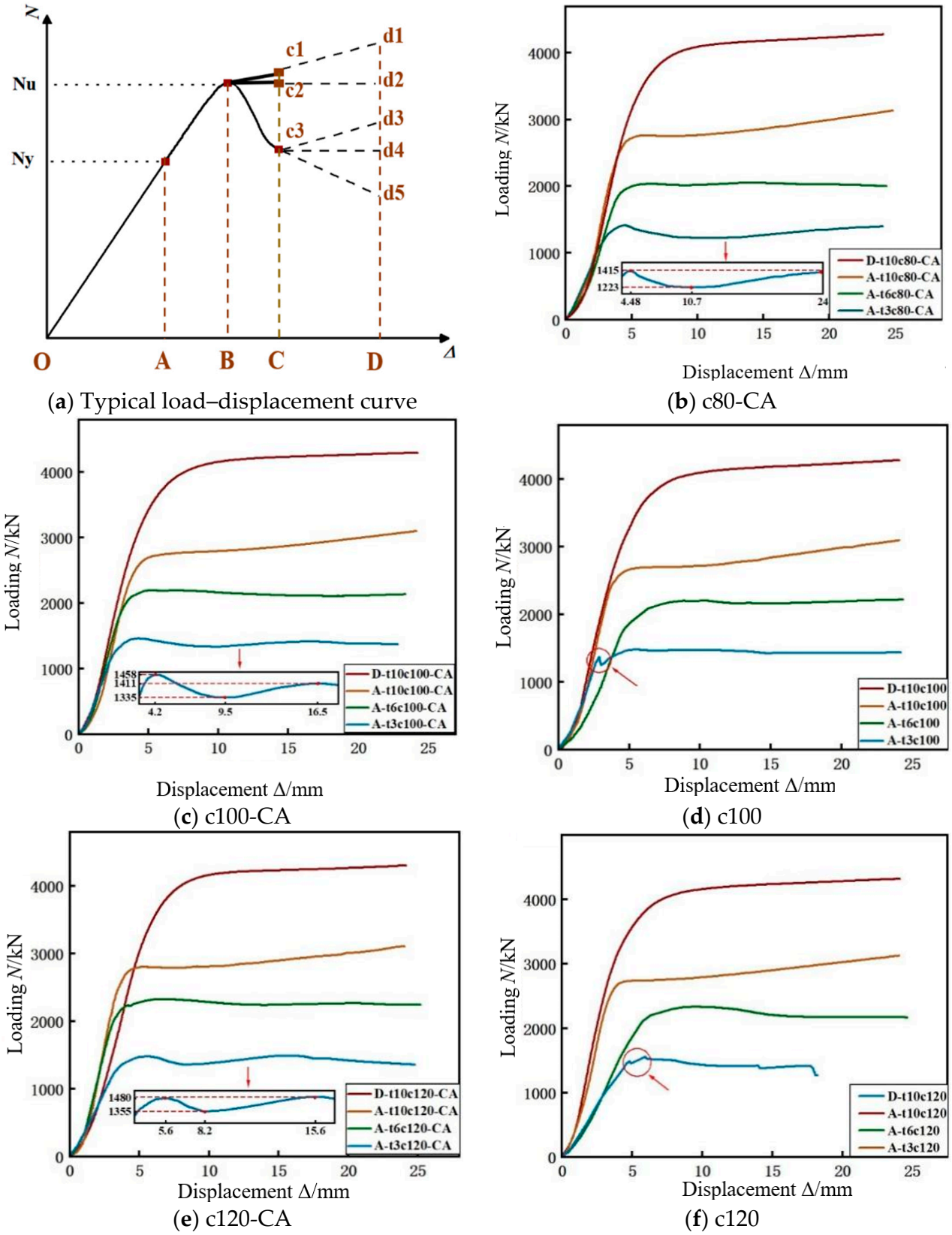

(**a**) Typical load–displacement curve (**b**) c80-CA

(**c**) c100-CA (**d**) c100

(**e**) c120-CA (**f**) c120

Figure 5. Load–displacement curves.

Table 5. Experimental results and performance indexes of specimens.

ID	Tangent Stiffness	*SCR*	α_{sc}	N_t/kN	Failure Type	ξ	*SI*	φ_{min}	*RR*
A-t3c80-CA	1282.67	5.16	0.13	1425.52	Shear	0.68	1.06	3.40%	0.92
A-t6c80-CA	1425.32	5.61	0.29	1459.78	Shear and bulging	1.63	1.11	3.80%	1
A-t10c80-CA	1972.33	5.79	0.56	1476.449	Bulging	3.26	1.09	3.90%	1.11
D-t10c80-CA	2105.51	9.00	0.56	1488.66	Bulging	5.07	1.26	5.80%	0.99
A-t3c100-CA	1304.37	4.69	0.13	1551.12	Shear	0.62	1.02	3.40%	0.97
A-t6c100-CA	1951.28	5.10	0.29	2034.75	Shear and bulging	1.49	1.15	3.80%	0.96
A-t10c100-CA	2128.05	5.26	0.56	2200.16	Bulging	2.96	1.10	3.90%	1.07
D-t10c100-CA	2463.14	8.19	0.56	2213.26	Bulging	4.6	1.23	5.80%	0.99
A-t3c100	1167.28	4.82	0.13	2330.6	Shear	0.64	1.05	3.40%	0.96
A-t6c100	1169.34	5.25	0.29	2334.3	Shear and bulging	1.53	1.17	3.80%	0.99
A-t10c100	1893.45	5.41	0.56	2700	Bulging	3.04	1.08	3.90%	1.1
D-t10c100	2272.13	8.42	0.56	2792	Bulging	4.74	1.21	5.80%	0.98
A-t3c120-CA	1208.33	4.44	0.13	2724.18	Shear	0.58	1.01	3.40%	0.99
A-t6c120-CA	1827.64	4.83	0.29	2800	Shear and bulging	1.41	1.19	3.80%	0.97
A-t10c120-CA	2273.29	4.98	0.56	2734.74	Bulging	2.8	1.09	3.90%	1.08
D-t10c120-CA	1890.32	7.75	0.56	4277.31	Bulging	4.36	1.22	5.80%	0.97
A-t3c120	1035.08	4.56	0.13	4297.45	Shear	0.6	1.07	3.40%	0.91
A-t6c120	1186.43	4.96	0.29	4279.2	Shear and bulging	1.44	1.21	3.80%	0.93
A-t10c120	2261.17	5.11	0.56	4323.89	Bulging	2.88	1.07	3.90%	1.11
D-t10c120	2589.46	7.96	0.56	4305.08	Bulging	4.47	1.20	5.80%	0.99

Note: *SCR* represents the stainless-steel-tube-to-concrete-strength ratio; α_{sc} denotes the steel content ratio; N_t represents ultimate bearing capacity; ξ is the confinement ratio; *SI* is the strength improvement factor; φ_{min} is the minimum axial shortening rate; *RR* is the residual strength residual rate.

Elastoplastic stage (segment AB): When the loading is between 70–80% of the ultimate load, the slope of the load–displacement curve gradually decreases. As the load and displacement continue to increase, the transverse deformation of the concrete gradually increases, and the stainless-steel tube begins to exert its confining effect. Due to the nonlinear roundhouse shape of the stress–strain curve of the stainless steel, the load–strain curve under the coordinated deformation of the stainless-steel tube and the core concrete exhibits more of a gradual yielding behavior at this stage. Comparing the experimental data of A-t10c120-CA with D-t10c120-CA and A-t3c120-CA with A-t10c120-CA, it can be seen that when the steel content ratio (α_{sc}) is similar, there is a 1% increase in the strength of the stainless-steel-tube-to-concrete-strength ratio (*SCR*) with an average increase of 0.98% in the ultimate bearing capacity. When the SCR is similar, a 1% increase in the steel content ratio of the specimen leads to an average increase of 0.27% in the ultimate bearing capacity (N_t). This indicates that an increase in the strength ratio has a more pronounced effect on enhancing the bearing capacity. Simultaneously, as the SCR and α_{sc} increase, the load–displacement curve becomes more round. The impact of the concrete strength enhancement on the bearing capacity is influenced by the confinement coefficient (ξ). Specifically, when the confinement coefficient (ξ) is approximately 0.6, a 1% increase in the SCR results in an average increase of 0.4% in N_t; when ξ is approximately 4.6, a 1% increase in the SCR leads to an average increase of 0.1% in Nt. According to Table 4, the incorporation of coarse aggregates has little impact on enhancing the bearing capacity but can effectively improve the small-scale sudden drops in the load–displacement curve before the ultimate load (which occur frequently when the thickness of the stainless-steel tube is 3 mm, as indicated by the arrows in Figure 5d,f), thus positively affecting the pre-peak ductility of the specimens.

Post-deformation stage (segment BC): In this stage, the core concrete developed through-cracks, leading to a decrease in its bearing capacity. Simultaneously, it squeezed the external stainless-steel tube, causing an increase in the hoop stress and a decrease in the axial stress of the tube, which correspondingly reduced the bearing capacity of the stainless-steel tube. On the other hand, the internal concrete exhibited an upward trend in bearing capacity due to confinement. Based on the varying amplitudes of positive and negative changes in the bearing capacities of the core concrete and the stainless-steel tube, three scenarios emerged: an increase in the bearing capacity of the test specimen (specimens

with a confinement coefficient (ξ) of 2.80–5.07), a stable bearing capacity (specimens with a confinement coefficient (ξ) of 1.41–1.63), and a decrease in the bearing capacity (specimens with a confinement coefficient (ξ) of 0.58–0.6), corresponding to c1, c2, and c3 in Figure 5a, respectively. Notably, the c3 scenario frequently occurs in diagonal shear failure. It is observed that when the thickness of the stainless-steel tube is 3 mm, there is a significant difference in the load–displacement curves between specimens with and without coarse aggregates. As indicated by the arrows in Figure 5b,c,e, the bearing capacity of specimens with coarse aggregates briefly drops after reaching the peak and then continues to rise. Moreover, as the concrete strength increases, both the downward and upward trends of the curve intensify, potentially related to the interference of coarse aggregates with the confinement mechanism of the stainless-steel tube on the concrete. The descending segment of the load–displacement curve after the peak is attributed to diagonal shear cracking of the core concrete. Due to the insufficient thickness of the stainless-steel tube, the core concrete was not effectively confined in a timely manner, resulting in a gradual decrease in the overall bearing capacity of the specimen until the confinement effect of the stainless-steel tube and the hoop expansion force of the core concrete reached equilibrium. The rigid skeleton formed by the coarse aggregates enhanced the cohesion of the matrix, acting as a bridging restraint against the development and propagation of micro- and macro-cracks, significantly reducing the hoop deformation of the concrete. This weakened and delayed the confinement effect of the stainless-steel tube. Additionally, the coarse aggregates contributed to maintaining a smooth and full load–displacement curve overall while flattening the descending segment. This is because the enhanced frictional resistance provided by the coarse aggregates present on the failure surface persisted as the cracked surface shifted. Even when the coarse aggregates were crushed, they provided additional resistance and mechanical interlocking on the shear plane. As the confinement coefficient (ξ) increases, the influence of coarse aggregates gradually diminishes. Comparing the duplex stainless-steel specimens with the austenitic specimens, both having a thickness of 10 mm, it can be seen that due to the higher yield strength of the duplex stainless steel, its ultimate bearing capacity is approximately 20% greater than that of the austenitic stainless steel.

Strengthening/weakening stage (segment CD): As the displacement gradually increases, the stainless-steel tube exhibits a phenomenon of stress strengthening. If the load–displacement curve rises after the peak, as in the c1 scenario, the slope of the rise gradually increases (e.g., A-t10c100-CA), corresponding to d1 in Figure 5a. If it follows the c3 scenario, where it initially drops, it will subsequently rise above the ultimate load (e.g., A-t3c120-CA), corresponding to d3 in Figure 5a. If the strengthening effect is not pronounced, this is classified as the weakening stage, manifested as the load–displacement curve entering a plateau (e.g., A-t6c100), corresponding to d2 and d4 in Figure 5a, or continues to decline (e.g., A-t3c100), corresponding to d5 in Figure 5a. If excessive deformation has occurred in the specimen before it rises again, the strengthening effect of the stainless-steel tube is structurally insignificant, and such situations should be avoided by adjusting the confinement coefficient. In comparison, the austenitic stainless steel exhibits better ductility, with an ultimate tensile strain reaching 50–60%, and its strengthening effect is more pronounced at larger deformations. On the other hand, the duplex stainless steel has a lower yield-to-tensile-strength ratio, resulting in a weaker strengthening effect in the later stages compared to the austenitic stainless steel. Compared to carbon steel, stainless-steel concrete columns retain a higher residual strength after experiencing greater axial loads and deformations.

3.3. Load–Strain Curve

The load–strain curve reflects the deformation characteristics of the stainless-steel tube and its confining effect on the core concrete. A typical load–strain curve is shown in Figure 6. In the initial loading stage, the test specimen was still in the elastic phase, where both the axial and hoop strains of the specimen increased linearly, with the axial strain developing at a faster rate. The ratio of hoop strain to axial strain does not show significant

growth and remains within the range of 2.7 to 3.3. At this point, the specimen was in the elastic phase, and both the core concrete and the stainless-steel tube bore the axial load together, with the stainless-steel tube providing no significant confining effect on the core concrete. As the specimen entered the elastoplastic phase, the strain measured at the center of the specimen's section was significantly greater than that at the corner measurement points, and the strain difference intensified with the development of local buckling, leading to an increasing trend in the ratio of hoop strain to axial strain. When the ratio of hoop strain to axial strain, representing the transverse deformation coefficient, exceeds Poisson's ratio (ν) of the stainless-steel material, the confining effect of the stainless-steel tube on the core concrete begins to manifest. For specimens with a confinement coefficient (ξ) of less than 1.1, the load–strain curve shows a significant descending segment after reaching the ultimate load (as shown in Figure 6a). For specimens with a confinement coefficient greater than 1.15, the curve descent is not pronounced or is absent (as shown in Figure 6b–d). At this point, the core concrete is crushed, further compressing the stainless-steel tube, which also indicates that the confining effect of the stainless-steel tube on the core concrete became increasingly stronger. A comparison of Figure 6 reveals that for D-t10c100-CA, at 30% of the ultimate load, the growth rate of strain gauge no. 5 is significantly faster than that in the linear growth stage (indicating the onset of the confining effect), and it reaches the nominal yield strain ($\varepsilon_{0.2}$) of the stainless-steel tube at around 65% of the ultimate load. This suggests that duplex stainless steel initiates confinement on the core concrete earlier and provides stronger confinement under the same axial load.

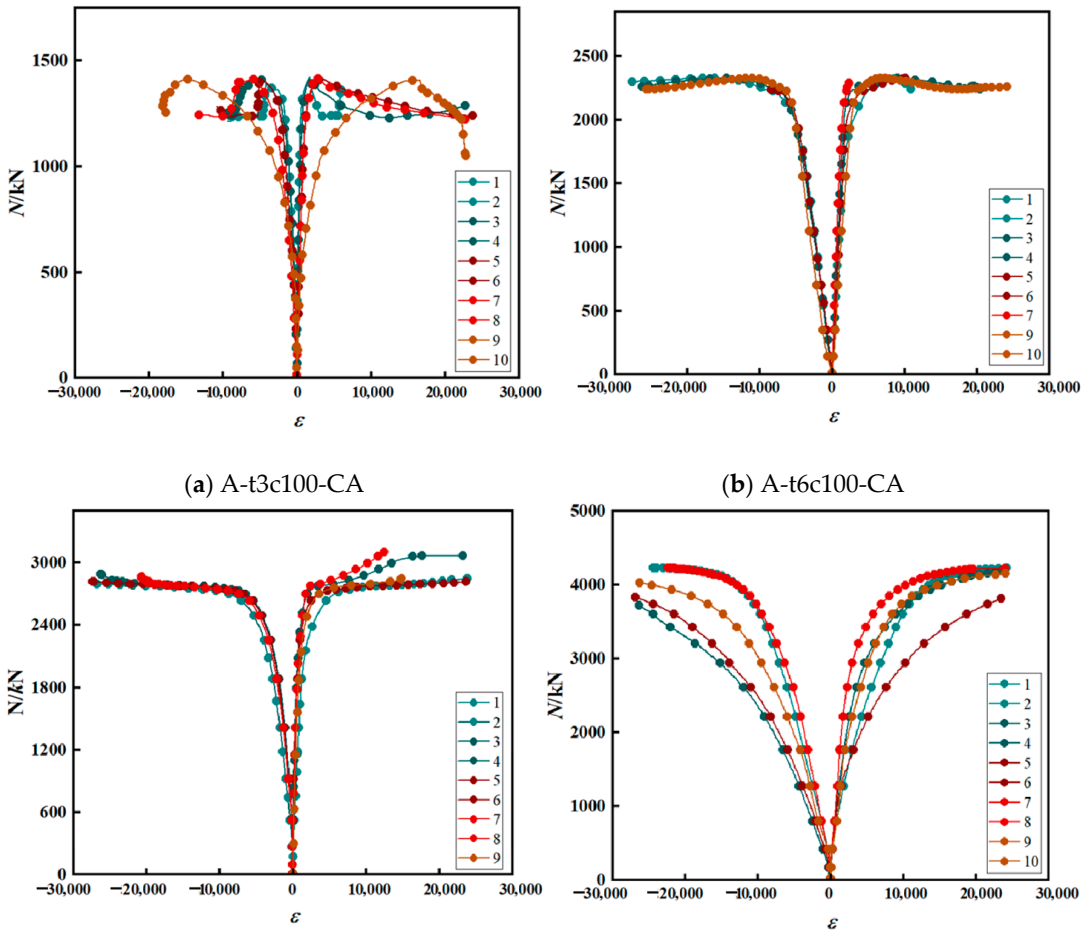

(**a**) A-t3c100-CA (**b**) A-t6c100-CA

(**c**) A-t10c100-CA (**d**) D-t10c100-CA

Figure 6. Load–strain curves.

4. Axial Compressive Performance

To investigate the effects of the coarse aggregate content and compressive strength of the core concrete, as well as the wall thickness and type of stainless steel, on the axial compressive bearing capacity of the CA-UFSST and UFSST specimens, the strength improvement factor and the residual strength residual rate of the concrete-filled steel tubes were employed to evaluate the axial compressive performance of the short-column specimens. Based on the experimental results, the influence of the confinement factor (ξ) on these two performance indicators was explored. The calculated values of the axial compressive bearing capacity indicators for each specimen are presented in Table 5. As shown in Equation (2), the confinement ratio (ξ), serving as a primary parameter to measure the interaction between the steel tube and concrete, is widely used to assess the confining capacity of the steel tube on the concrete. This factor is crucial in axial compression tests, as it directly influences the failure mode and bearing capacity of the specimens. The high confinement ratio usually means that the steel tube can effectively restrain the deformation of the concrete, thereby improving the bearing capacity and ductility of the UFSST. In engineering practice, the confinement ratio can be adjusted to meet the specific structural performance requirements by designing the section size and thickness of the steel tube reasonably and selecting the appropriate concrete strength grade.

$$\xi = \frac{A_s f_y}{A_c f_{ck}} \tag{2}$$

where A_s and A_c represent the area of the steel tube and the area of the core concrete, respectively, with their units expressed in mm^2; f_y and f_{ck} denote the nominal yield strength of the stainless-steel tube and the axial compressive strength of the core concrete, respectively, with their units expressed in MPa.

4.1. Strength Improvement Factor

This paper introduces the strength improvement factor (*SI*) to measure the composite effect between a stainless-steel tube and core concrete [6]. The formula is presented as Equation (3):

$$SI = N_t / (A_s \sigma_{0.2} + A_c f_{ck}) \tag{3}$$

where N_t is the measured ultimate bearing capacity of the short column, and $\sigma_{0.2}$ and f_{ck} denote the nominal yield strength of the stainless-steel tube and the axial compressive strength of the core concrete, respectively.

The relevant indicators for the various specimens are shown in Table 5, with the SI values for CA-UFSST and UFSST ranging from 1.01 to 1.26 and 1.05 to 1.21, respectively. The SI values for all specimens are greater than 1, indicating that the stainless-steel tube and the core concrete exhibit good bearing capacity. As shown in Figure 7a, the SI of both the CA-UFSST and UFSST specimens is generally positively correlated with the confinement coefficient. Notably, for CA-UFSST, the transition from predominantly shear failure to bulging failure occurs around a confinement coefficient of approximately 1.5. This transition point signifies a significant change in the failure mechanism, where the confinement provided by the stainless-steel tube becomes sufficient to restrict lateral deformation and promote bulging failure. When the confinement coefficient of the specimen is less than 2, the SI of UFSST is higher than that of CA-UFSST; when the confinement coefficient is greater than 2, the SI of CA-UFSST is higher than that of UFSST. This suggests that the confinement coefficient had a greater impact on the bearing capacity performance of CA-UFSST, and CA-UFSST required a larger confinement coefficient to exert a better combination effect. The reason for this phenomenon may be that the confining effect of CA-UFSST occurred later, corresponding to a higher load, and the lateral deformation rate of the core concrete was excessive. If the confinement coefficient is too small, it cannot effectively restrict the rate of lateral deformation of the core concrete in a timely manner, which may immediately lead to diagonal shear failure, resulting in the failure of CA-UFSST.

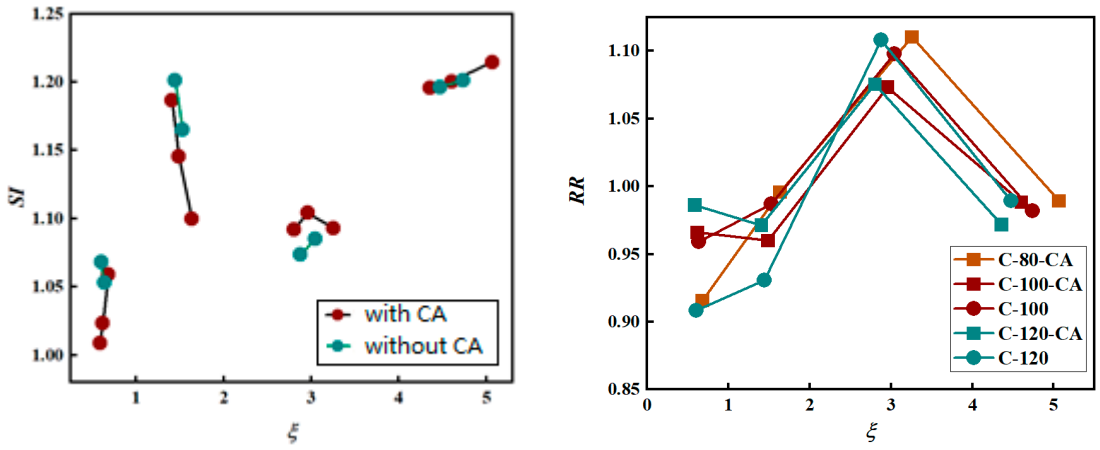

(**a**) *SI* (**b**) *RR*

Figure 7. Bearing capacity index of specimens.

4.2. Ductile Index

Improved ductility is another significant aspect reflecting the synergistic work between a stainless-steel tube and core concrete. In this paper, the residual strength residual rate (*RR*) is used to assess ductility. The formulas are presented as Equations (4) and (5):

$$\varphi_{\lim} = \frac{\Delta L_{\lim}}{L} = 15\frac{f_y}{E_s} \tag{4}$$

$$RR = \frac{N_r}{N} \tag{5}$$

where $\varphi_{\lim}$ is the ultimate axial shortening rate of the short column; $\Delta L_{\lim}$ is the minimum axial shortening limit of the short column; L is the calculated length of the short column; and N_r is the residual strength of the short column, which refers to the strength beyond the minimum axial shortening limit.

As shown in Figure 7b, the *RR* values for all specimens fall within the range of 0.9 to 1.1, which are all greater than the minimum value for the safe design of residual strength, i.e., 70% of the design bearing capacity. This indicates that the structural performance meets the ductility requirements and can ensure that the specimens maintain a significant residual bearing capacity even under large axial deformations. Among them, the specimens with 10 mm-thick austenitic stainless-steel tubes exhibit residual strengths (N_r) that even exceed the ultimate bearing capacity, with their *RR* values ranging from 1 to 1.1, which is 10% higher than those of the duplex stainless-steel tubes of the same thickness. This is attributed to the more pronounced strain-hardening effect of the austenitic stainless steel. Although the duplex stainless steel has a higher yield strength, ensuring a higher ultimate bearing capacity for the specimens, its ratio of ultimate strength to yield strength is relatively low, and the rate of increase in the later stage of the stress–strain curve is relatively small. Even when the circumferential deformation of the concrete intensified in the later stage, it did not significantly enhance the confining effect of the stainless-steel tube. Therefore, the load–displacement curve of the duplex stainless-steel specimens remains stable at a consistently high level.

5. Comparisons Between Analytical Model and Experimental Results

As mentioned in the previous section, the existing design specifications for the axial compressive bearing capacity of CFST includes a Chinese specification (CECS 159:2004, GB 50936-2014 and DBJ/T13-51-2020), a European specification (EC4), and an American specification (ACI 318-05 and AISC 360). These specifications impose certain limits on the maximum values of a steel tube and concrete strength. Whether they can be directly applied

to predict the bearing capacity of UFSSTs needs to be verified. The formulas, applicable scopes, and calculation results of the aforementioned specifications are presented in Table 6.

Table 6. Comparison between experimental results and analytical results.

Codes	Analytical Model	μ	MAPE
CECS 159:2004 [28]	$N_u = A_s \cdot f_y + A_c \cdot f_{ck}$	0.89	0.014
DBJ/T13-51-2020 [29]	$N_u = A_{sc} \cdot (1.18 + 0.85\xi) \cdot f_{ck}$	1.19	0.044
GB 50936-2014 [30]	$N_u = A_{sc} \cdot f_{sc}$ $f_{sc} = (1.212 + B\xi + C\xi^2) \cdot f_{ck}$ $B = 0.131\frac{f_y}{213} + 0.273$ $C = -0.070\frac{f_y}{14.4} + 0.026$	0.65	0.13
EC4 [31]	$N_u = A_s \cdot f_y + A_c \cdot f_y^{'}$	0.92	0.01
ACI 318-05 [32]	$N_u = A_s \cdot f_y + 0.85A_c \cdot f_y^{'}$	0.86	0.019
AISC 360 [33]	$N_u = A_s \cdot f_y + 0.85A_c \cdot f_y^{'}$	0.86	0.019

Note: μ = mean value of the ratio of calculated to measured results; MAPE = mean absolute percentage error.

Among these, the prediction error of the Chinese specification (GB 50936-2014) is greater than 10%, and when the confinement factor (ξ) exceeds 1.63, the results become negative, which does not align with the actual situation. The mean values (μ) of the ratios of the calculated results to the measured values for EC4, AISC/ACI, DBJ, and CECS are 0.92, 0.86, 1.19, and 0.89, respectively, with the mean absolute percentage errors (MAPEs) of 0.010, 0.019, 0.044, and 0.014, respectively. Through a comparison, it can be seen that the prediction results of EC4, AISC/ACI, and CECS, which employ the superposition principle, are conservative, as they do not account for the enhancement in the bearing capacity performance due to the interaction between the steel tube and the core concrete. The prediction results of DBJ are higher than the actual values, which may pose safety risks if applied in practical situations. The prediction errors in the existing codes can be attributed to several factors. Firstly, codes such as CECS, ACI, and AISC adopt the superposition principle, which does not fully account for the synergistic effect between the stainless-steel tube and the core concrete, leading to conservative predictions. Secondly, codes like GB 50936-2014 and DBJ, which are based on the unified theory, may overestimate the bearing capacity due to the simplifications of their models. Finally, as the confinement ratio increases, the confining effect of the stainless-steel tube becomes more significant, but this effect is often neglected in the existing codes, resulting in increased prediction errors, particularly for the duplex stainless-steel specimens.

To enhance the robustness of the conclusions, a statistical analysis using an analysis of variance (ANOVA) was conducted on the experimental data. The results indicate that the confinement ratio, stainless-steel type, and concrete strength all have significant effects on the axial compressive performance of the specimens ($p < 0.05$). Specifically, the confinement factor has the most pronounced effect, followed by the stainless-steel type and concrete strength. The ANOVA analysis supports the findings presented in the previous sections and further validates the need for a more accurate calculation model for the axial compressive bearing capacity of CA-UFSST and UFSST. EC4 exhibits the best prediction performance, with an average error of approximately 8%. However, as the confinement factor increases, the deviation caused by ignoring the confining effect gradually enlarges, leading to a noticeable lack of accuracy in predicting the behavior of duplex stainless-steel specimens, with an average error exceeding 15%. Therefore, the current specifications have certain limitations in predicting the behavior of CA-UFSST and UFSST. It is necessary to establish a more accurate formula for calculating the axial compressive bearing capacity based on theoretical derivations and the selection of an appropriate confined-concrete calculation model.

6. Conclusions

This paper conducted an experimental study on the axial compressive performance of square CA-UHSST (Concrete-filled Aluminum Ultra-High-Strength Steel Tube) and UHSST (Ultra-High-Strength Steel Tube) short-column specimens. It explores the mechanical mechanism of the short columns through investigations into failure modes, load–displacement curves, load–strain curves, and load–Poisson's ratio curves. Furthermore, multiple methods were employed to predict the bearing capacity of the specimens, leading to the following conclusions:

(1) CA-UFSST (Concrete-filled Aluminum Ultra-High-Strength Steel Tube) and UFSST (Ultra-High-Strength Steel Tube) exhibit a good deformation capacity under axial compressive loading, and the failure modes of their core concrete are both related to the confinement factor. For specimens with a small confinement factor (0.38–0.58), diagonal shear failure of the concrete is evident. For specimens with a medium confinement factor (0.85–1.28), both diagonal shear failure and barrel-shaped failure occur, with the degree of failure being slightly less severe than that of diagonal shear failure. For specimens with a large confinement factor (1.64–3.2), varying degrees of circumferential bulging or expansion were observed, manifesting as barrel-shaped failure.

(2) The addition of coarse aggregates increases the stiffness of the specimens by approximately 1.27 times and raises the load corresponding to the end of the elastic stage from about 70% to 80% of the ultimate load. For specimens with a small confinement factor (0.38–0.58), coarse aggregates weaken and delay the confining effect of the stainless-steel tube.

(3) The strength improvement factor of the bearing capacity is positively correlated with the confinement factor (ξ). For CA-UFSST (Concrete-filled Austenitic Ultra-High-Strength Steel Tube), a confinement factor greater than 2 is required to exhibit a more favorable composite effect compared to UFSST. Due to differences in the strength-to-yield ratio, the ductility index of specimens with a 10 mm-thick austenitic stainless-steel tube is 10% higher than that of specimens with a 10 mm-thick duplex stainless-steel tube.

(4) Comparing the experimental results with the calculation formulas in current codes, it was found that the prediction error of the Chinese code (GB 50936-2014) exceeds 10%, while the predictions of EC4, AISC/ACI, and CECS are conservative. EC4 provides the best prediction, with an average error of approximately 8%. However, as the confinement factor increases, the deviation caused by neglecting the confining effect gradually enlarges, leading to a significant lack of accuracy in predicting the behavior of duplex stainless-steel composite specimens, with an average error exceeding 15%. Therefore, there is a need to establish more accurate formulas for calculating the axial compressive bearing capacity of CA-UFSST and UFSST in the future.

(5) The results demonstrate the potential benefits of using UHPC and stainless-steel tubes in structural applications. Practically, UHPC-filled stainless-steel tubes offer improved durability and corrosion resistance compared to traditional materials, making them suitable for harsh environments. While the initial cost may be higher, the long-term cost savings from reduced maintenance and an extended service life could justify investments. Additionally, the ease of implementation in construction projects is facilitated by the improved workability of UHPC and the precision fabrication of stainless-steel tubes.

Author Contributions: W.L.: conceptualization, funding acquisition, project administration, and resources. M.Z.: data curation, formal analysis, investigation, and writing—original draft. G.L.: supervision, software, and validation. Y.H.: project administration and methodology. B.W.: supervision and writing—review and editing. Y.C.: data curation, investigation, and validation. W.H.: investigation, validation, and writing—review and editing. H.L.: formal analysis and investigation. Z.T.: software

and investigation. Y.Z.: funding acquisition, project administration, supervision, writing—review and editing. All authors have read and agreed to the published version of the manuscript.

Funding: This study was sponsored by the Xihua University Project (Z231001 and H242201).

Data Availability Statement: Data will be made available on request.

Conflicts of Interest: Authors Wenrui Li, Guo Li, Yang Hu, Bei Wang and Yongfei Cao were employed by the company The First Construction Engineering Limited Company of China Construction Third Engineering Bureau (Sichuan Branch). Author Mengqi Zhu was employed by the company Dongfang Boiler Co., Ltd. The remaining authors declare that the research was conducted in the absence of any commercial or financial relationships that could be construed as a potential conflict of interest.

References

1. Wang, X.; Fan, F.; Lai, J. Strength behavior of circular concrete-filled steel tube stub columns under axial compression: A review. *Constr. Build. Mater.* **2022**, *322*, 126144. [CrossRef]
2. Niyirora, R.; Niyonyungu, F.; Hakuzweyezu, T.; Masengesho, E.; Nyirandayisabye, R.; Munyaneza, J. Behavior of concrete-encased concrete-filled steel tube columns under diverse loading conditions: A review of current trends and future prospects. *Cogent Eng.* **2023**, *10*, 2156056. [CrossRef]
3. Tang, H.; Wang, H.; Liu, R.; Zou, X.; Jia, Y. Axial compression behavior of CFRP-confined square concrete-filled double skin tube stub columns with stainless steel outer tube. *Ocean Eng.* **2022**, *266*, 112871. [CrossRef]
4. Yan, J.; Chen, A.; Zhu, J. Behaviours of square UHPFRC-filled steel tubular stub columns under eccentric compression. *Thin-Walled Struct.* **2021**, *159*, 107222. [CrossRef]
5. Wei, J.; Xie, Z.; Zhang, W.; Luo, X.; Yang, Y.; Chen, B. Experimental study on circular steel tube-confined reinforced UHPC columns under axial loading. *Eng. Struct.* **2021**, *230*, 111599. [CrossRef]
6. Chen, S.; Zhang, R.; Jia, L.; Wang, J.; Gu, P. Structural behavior of UHPC filled steel tube columns under axial loading. *Thin-Walled Struct.* **2018**, *130*, 550–563. [CrossRef]
7. Guler, S.; Copur, A.; Aydogan, M. Axial capacity and ductility of circular UHPC-filled steel tube columns. *Mag. Concr. Res.* **2013**, *65*, 898–905. [CrossRef]
8. Xu, L.; Lu, Q.; Chi, Y.; Yang, Y.; Yu, M.; Yan, Y. Axial compressive performance of UHPC filled steel tube stub columns containing steel-polypropylene hybrid fiber. *Constr. Build. Mater.* **2019**, *204*, 754–767. [CrossRef]
9. Le Hoang, A.; Fehling, E.; Thai, D.; Van Nguyen, C. Evaluation of axial strength in circular STCC columns using UHPC and UHPFRC. *J. Constr. Steel Res.* **2019**, *153*, 533–549. [CrossRef]
10. Yu, M.; Liao, W.; Liu, S.; Wang, T.; Yu, C.; Cheng, S. Axial compressive performance of ultra-high performance concrete-filled steel tube stub columns at different concrete age. *Structures* **2023**, *55*, 664–676. [CrossRef]
11. Ye, Y.; Li, W.; Guo, Z. Performance of concrete-filled stainless steel tubes subjected to tension: Experimental investigation. *Thin-Walled Struct.* **2020**, *148*, 106602. [CrossRef]
12. Gardner, L. Stability and design of stainless steel structures—Review and outlook. *Thin-Walled Struct.* **2019**, *141*, 208–216. [CrossRef]
13. Baddoo, N. Stainless steel in construction: A review of research, applications, challenges and opportunities. *J. Constr. Steel Res.* **2008**, *64*, 1199–1206. [CrossRef]
14. Francis, R.; Byrne, G. Duplex Stainless Steels—Alloys for the 21st Century. *Metals* **2021**, *11*, 836. [CrossRef]
15. Rezayat, M.; Karamimoghadam, M.; Moradi, M.; Casalino, G.; Rovira, J.R.; Mateo, A. Overview of Surface Modification Strategies for Improving the Properties of Metastable Austenitic Stainless Steels. *Metals* **2023**, *13*, 1268. [CrossRef]
16. Young, B.; Ellobody, E. Experimental investigation of concrete-filled cold-formed high strength stainless steel tube columns. *J. Constr. Steel Res.* **2006**, *62*, 484–492. [CrossRef]
17. Ellobody, E.; Young, B. Design and behaviour of concrete-filled cold-formed stainless steel tube columns. *Eng. Struct.* **2006**, *28*, 716–728. [CrossRef]
18. Lam, D.; Gardner, L. Structural design of stainless steel concrete filled columns. *J. Constr. Steel Res.* **2008**, *64*, 1275–1282. [CrossRef]
19. Tao, Z.; Song, T.; Uy, B.; Han, L. Bond behavior in concrete-filled steel tubes. *J. Constr. Steel Res.* **2016**, *120*, 81–83. [CrossRef]
20. Dai, P.; Yang, L.; Wang, J.; Lin, M.; Fan, J. Bond stress-slip relationship in concrete-filled square stainless steel tubes. *Constr. Build. Mater.* **2022**, *326*, 127001. [CrossRef]
21. Xiong, M.; Liew, J.; Wang, Y.; Xiong, D.; Lai, B. Effects of coarse aggregates on physical and mechanical properties of C170/185 ultra-high strength concrete and compressive behaviour of CFST columns. *Constr. Build. Mater.* **2020**, *240*, 117967. [CrossRef]
22. Güneyisi, E. Axial compressive strength of square and rectangular CFST columns using recycled aggregate concrete with low to high recycled aggregate replacement ratios. *Constr. Build. Mater.* **2023**, *367*, 130319. [CrossRef]
23. Wu, F.; Xu, L.; Zeng, Y.; Yu, M. Experimental investigation of axially loaded circular ultra-high performance concrete with coarse aggregate (CA-UHPC) filled steel tube slender columns. *Structures* **2023**, *58*, 105355. [CrossRef]
24. *GB/T228.1-2010*; Metallic Materials-Tensile Testing-Part 1: Method of Test at Room Temperature. China Standard Press: Beijing, China, 2010.

25. *GB/T50081-2019*; Standard for Test Methods of Concrete Physical and Mechanical Properties. China Construction Industry Press: Beijing, China, 2019.
26. Han, L. Tests on stub columns of concrete-filled RHS sections. *J. Constr. Steel Res.* **2002**, *58*, 353–372. [CrossRef]
27. Du, Y.; Chen, Z.; Xiong, M. Experimental behavior and design method of rectangular concrete-filled tubular columns using Q460 high-strength steel. *Constr. Build. Mater.* **2016**, *125*, 856–872. [CrossRef]
28. *CECS159:2004*; Technical Specification for Structures with Concrete-Filled Rectangular Steel Tube Members. China Planning Press: Beijing, China, 2004.
29. *DBJ/T13-51-2020*; Technical Specification for Concrete-Filled Steel Tubular Structures. Department of Housing and Urban-Rural Development of Fujian Province Press: Fuzhou, China, 2020.
30. *GB50936-2014*; Technical Code for Concrete Filled Steel Tubular Structures. China Construction Industry Press: Beijing, China, 2014.
31. Hendy, C.; Johnson, R. *Designers' Guide to Eurocode 4: Design of Composite Steel and Concrete Structures*; Thomas Telford: Bristol, UK, 2006.
32. *ACI318-08*; Building Code Requirements for Structural Concrete (ACI 318-08) and Commentary. American Concrete Institute: Mumbai, India, 2008.
33. Titus, H.; Jayachandran, S. Three-dimensional frame buckling benchmark problems for direct analysis method in ANSI/AISC 360-16. In Proceedings of the Annual Stability Conference, Structural Stability Research Council, Denver, CO, USA, 22–25 March 2022.